ORIGINAL PAPER

Influence of Zn²⁺ Doping on CaFe₂O₄ Spinel Ferrites: An Analysis of Experimental Charge Density and Magnetism

M. Charles Robert[1] · M. Thavarani[2] · N. Pavithra[2] · S. Balaji Prasath[1] · R. Saravanan[3] · Y. B. Kannan[4]

Abstract

Single-phase, nanocrystalline Zn^{2+} substituted cubic spinel $CaFe_2O_4$ with the composition $Zn_xCa_{1-x}Fe_2O_4$ ($x=0.0, 0.05, 0.1, 0.15$) was prepared by solvothermal method. The magnetic properties of the prepared samples were analysed by vibration sample magnetometer (VSM), which reveals a switching from soft ferromagnetic behaviour to super-paramagnetic for an increase in Zn^{2+} doping concentration. The maximum coercivity of 405.54 G and squareness ratio of 35.8% is obtained for pure $CaFe_2O_4$, and the doping of nonmagnetic Zn^{2+} ions gradually loses the ferromagnetism. Neel's two sublattices' collinear model well explains the overall magnetic property. The surface morphology and elemental composition were analysed using scanning electron microscopy (SEM) and energy-dispersive X-ray (EDX) analysis. An optical bandgap analysis was carried out using UV–Visible spectroscopy, revealing a random variation of the optical energy gap with composition. X-ray peak analysis reveals the single-phase cubic spinel structure with Fd-3 m space group. The estimated crystallite sizes range from 22 to 39 nm, and lattice parameter varies in random fashion with the increase of Zn^{2+} doping concentration. Mixed cubic spinel structure is revealed from cation distribution analysis. Rietveld refinement technique is utilised for structural refinements. The maximum entropy method (MEM) is used for the experimental electron density analysis and hence bonding. The 3D, 2D and 1D MEM analyses reveal the weakest tetrahedral A–tetrahedral A bonding and the alteration in tetrahedral A–octahedral B and octahedral B–octahedral B bond strength with doping. Moderate A–O and B–O covalent bonding favours maximum saturation magnetism of 83.59 emu/g for the composition $Zn_{0.05}Ca_{0.95}Fe_2O_4$.

1 Introduction

The search for new magnetic materials with remarkable magnetic properties is of everlasting interest because of its industrial and scientific applications such as sensing, recording, biomedical and imaging applications [1–3]. A wide range of magnetic materials is devised by modifying the synthesis method, cation distribution, sintering temperature and nature and concentration of dopants [4–7]. The challenges in understanding spinel ferrites include the microstructural distribution of electrons, bonding nature and super exchange interaction between (tetrahedral) A and (octahedral) B sites [8, 9].

Calcium ferrite is one of the least reported cubic spinel ferrites because of its high ionic radius [10]. Calcium ferrite prepared by chemical precipitation method using NaOH precipitating agent was reported to have a magnetic moment of 1.74 emu/g and magnetic coercivity of 35.08 G for superparamagnetic applications [11]. Zinc ferrite is an extensively studied material because of its magnetic properties and uses [12]. The nanoparticles (5 to 20 nm) of $CaFe_2O_4$ prepared by the auto-combustion method was reported to have magnetic saturation (Ms), 31.1 emu/g [13]. *Lavanya Khanna* and *N. K. Verma* reported the magnetic properties with the size

✉ M. Charles Robert
jothycharles@gmail.com

1   Research Centre and PG, Department of Physics, Hajee Karutha Rowther Howdia College, Uthamapalayam, Tamil Nadu, India

2   Department of Physics, Sri Adi Chunchanagiri Women's College, Cumbum, Tamil Nadu, India

3   Research Centre and PG, Department of Physics, Madura College, Madurai, Tamil Nadu, India

4   Department of Physics, Arumugam Pillai Seethai Ammal College, Tiruppattur, Tamil Nadu, India

effect at different calcination temperatures (nano-capsule along (0 4 0) direction at 900 °C and nanosphere at 500 °C) [14]. The magnetic hyperthermia applications of nanometric size (12–14 nm), $Zn_{0.5}Ca_{0.5}Fe_2O_4$ for cancer treatment, were reported by *Rosario Argentina Jasso-Teran* [15]. Normally, $ZnFe_2O_4$ is a normal ferrite, whereas $CaFe_2O_4$ is an inverse ferrite with divalent Zn^{2+} occupying tetrahedral A site and divalent Ca^{2+} occupying both tetrahedral A and octahedral B site [16, 17]. The proper incorporation of divalent nonmagnetic Zn^{2+} in $CaFe_2O_4$ can tune the magnetic saturation and coercivity [18], which two theoretical models can explain, Neel's two sublattice model [19] and noncollinear magnetic spin canting model [20].

Though calcium ferrite is a vital metal oxide that is environmentally safe, chemically stable, low cost and enormously abundant, the overall literature survey confirms that $CaFe_2O_4$ is one of the least studied cubic spinel ferrites. Further, most of the research articles emphasise the synthesis, physical, optical and magnetic properties. No reported work revealed an experimental microstructural analysis of the Zn-doped $CaFe_2O_4$ spinel ferrites like structure factor, charge density distribution and inter-bonding behaviour. The success of MEM methodology adopted for the electron density distribution analysis for different application-oriented materials like bulk ceramics, piezoelectric ceramics, ferrites and dilute magnetic semiconductors was reported by various researchers [21–24].

Hence, in the first phase of the work, the synthesis of Zn^{2+} doping on $CaFe_2O_4$ ($Zn_xCa_{1-x}Fe_2O_4$, $x = 0.0, 0.05, 0.1, 0.15$) by solvothermal method and their analysis of magnetism, optical bandgap, surface morphology and elemental composition using vibration sample magnetometer (VSM), UV–Visible spectrometer, SEM and EDX, respectively were given importance. In the second phase, computational structural analysis using the Rietveld refinement technique [25] and charge density distribution using the maximum entropy method (MEM) [26] were performed using the precise experimental X-ray diffraction data.

2 Experimental Details

2.1 Material Synthesis

The spinel ferrite nanoparticles of all compositions, $Zn_xCa_{1-x}Fe_2O_4$ ($x = 0.0, 0.05, 0.1, 0.15$), were synthesised using a cost-effective low-temperature solvothermal method, methodology followed by *Abbas Kheradmand* et al. [27]. This synthesis method has advantages like high purity, chemical homogeneity, small and uniform particle size and controlled particle size [28, 29]. The starting materials used for the synthesis are $Zn(NO_3)_2.6H_2O$, $Fe(NO_3)_3.9H_2O$,

$Ca(NO_3)_2.4H_2O$, ethylene glycol, NaOH and HCl acid, purchased from Sigma Aldrich, India.

2.2 Experimental Techniques

The prepared compositions of the samples were ground well, using mortar and pestle and sieved using 400 nylon mesh for powder X-ray diffraction analysis at temperature, 25 °C. X-ray diffraction data were collected using Bruker AXS D8 advance X-ray diffractometer. This instrument is designed with TWIN/TWIN switching between four different instrument geometries for the analysis of powder diffraction to amorphous and thin film analysis. The primary TWIN optic implements a motorised divergence slit for Bragg–Brentano geometry and a Gobel mirror for parallel beam geometry, whereas the secondary TWIN optic features motorised antiscatter slit for Bragg–Brentano and an equatorial Soller slit for parallel beam geometry. The anode material used for powder diffraction is copper (Cu) with $K_{\alpha 1}$ and $K_{\alpha 2}$ radiation of wavelengths $\lambda_1 = 1.5406$ Å and $\lambda_2 = 1.54443$ Å ($K_{\alpha 1}$/ $K_{\alpha 2} = 0.5$) powered by the generator with 15 mA of current and 40 kV potential. The size of the divergent slit was 0.9167°, and the goniometer radius was fixed as 145 mm. The scanning angle 2θ was set from 10° to 120° with step size nearly 0.02°. The surface morphology (SEM) and elemental composition (EDX) were analysed using TESCAN VEGA3 SPH. The optical parameter (optical bandgap) was analysed using a UV–Visible spectrometer, model-JASCO V-630, with wavelength ranges from 2000 Å to 8000 Å. The room temperature magnetic hysteresis property of the samples was analysed using a vibration sample magnetometer (Lakeshore) with a maximum applied magnetic field of 1.5 T.

2.3 Computational Techniques

The essential structural parameters of the crystalline unit cell-like lattice parameters and oxygen occupational parameters were elucidated using the powder profile fitting methodology by Rietveld method [25] using the software JANA2006 [30]. The bond length between cations and cations (Me-Me) and cations and anions (Me-O), bond angles, tetrahedral and octahedral radius, shared and unshared edge length and hopping length were calculated using cation distribution analysis by Bertaut method [31, 32].

The Rietveld refined structure factor of various (h k l) planes was utilised for the electron density distribution analysis using the maximum entropy method. The entire unit cell is divided into ($128 \times 128 \times 128$) pixels along three lattice axes ($a = b = c$), and a uniform initial electron density in each pixel is fixed as F_{000}/a^3; F_{000} is the number of electrons in the unit cell and a lattice parameter. The Lagrangian multiplier is suitably fixed for convergence with a lesser number

of iterations. The MEM-based electron density distribution is visualised using VESTA [33]. 3D and 2D images of the electron density distribution with structure in different iso-surface levels and numerical 1D profile between different bonding ions were analysed using VESTA.

3 Results and Discussion

3.1 Experimental Analysis

3.1.1 X-ray Diffraction Analysis

X-ray diffraction intensity data of all the prepared samples of $Zn_xCa_{1-x}Fe_2O_4$ ($x = 0.0, 0.05, 0.1, 0.15$) shows the prominent peaks (202), (311), (222), (400), (422), (511) and (440) corresponding to cubic spinel ferrites (space group $F_{d-3 m}$), confirming the formation of spinel structure. No additional peaks were detected showing single-phase formation except the peaks emerging from Cu-K_α doublet $K_{\alpha1}$ and $K_{\alpha2}$ X-ray radiation of wavelengths $\lambda_1 = 1.5406$ Å and $\lambda_2 = 1.54443$ Å, which dominate the compositions $x = 0.1$ and $x = 0.15$. All composition of the samples has high-intensity peaks showing good crystallinity of the prepared samples.

Figure 1 shows a shift in the X-ray intensity peaks for the prominent peaks (113), (004), (115) and (404), which shows a small shift in 2θ towards the lower angles as the Zn^{2+} doping increases up to $x = 0.1$. This may be due to the doping of lower ionic radii dopant ($Zn^{2+} = 0.74$ Å) in higher ionic radii host atoms ($Ca^{2+} = 0.99$ Å) [34]. The sample with $x = 0.15$ composition has a small shift in 2θ towards the higher angle, which is due to a slight lattice disorder.
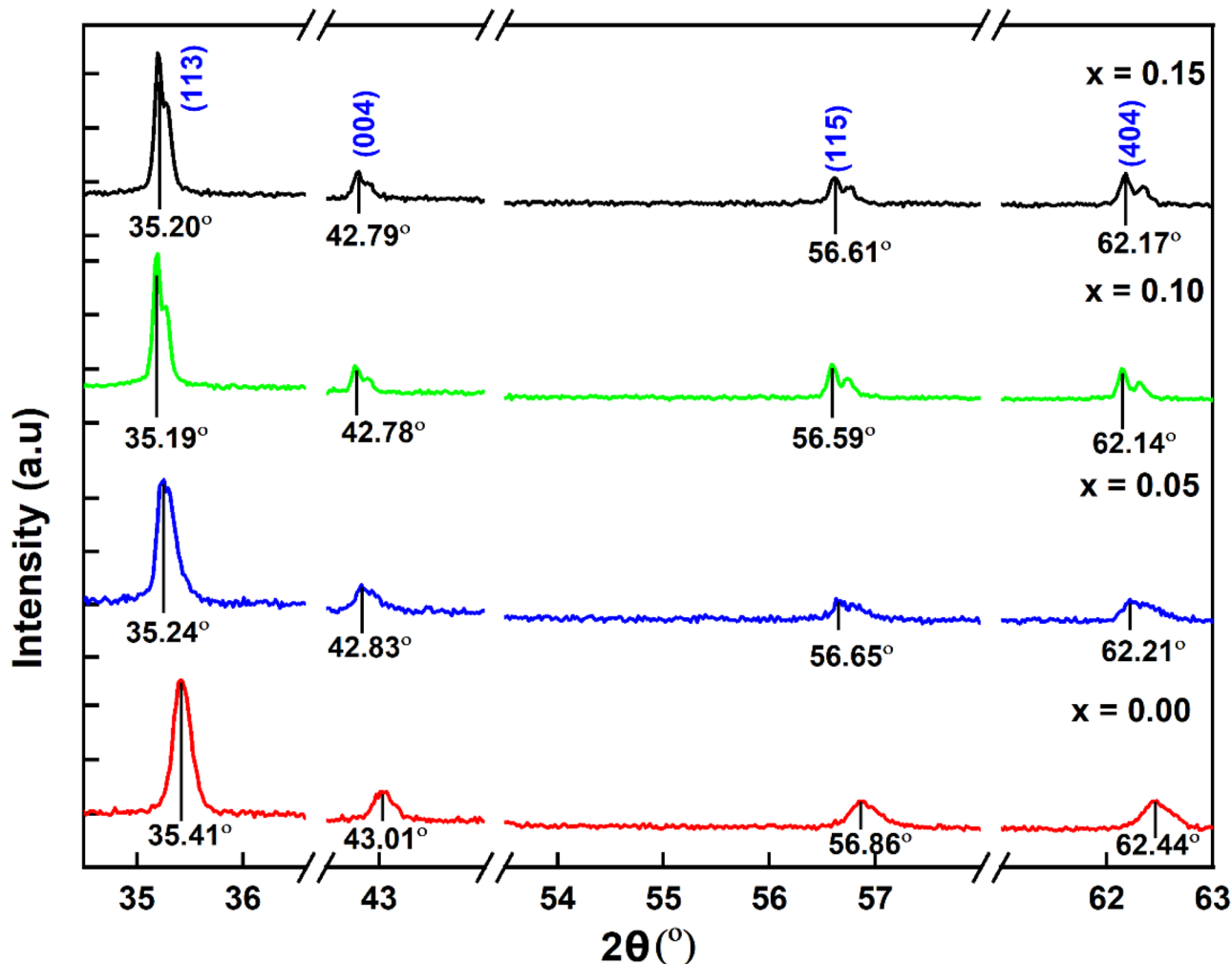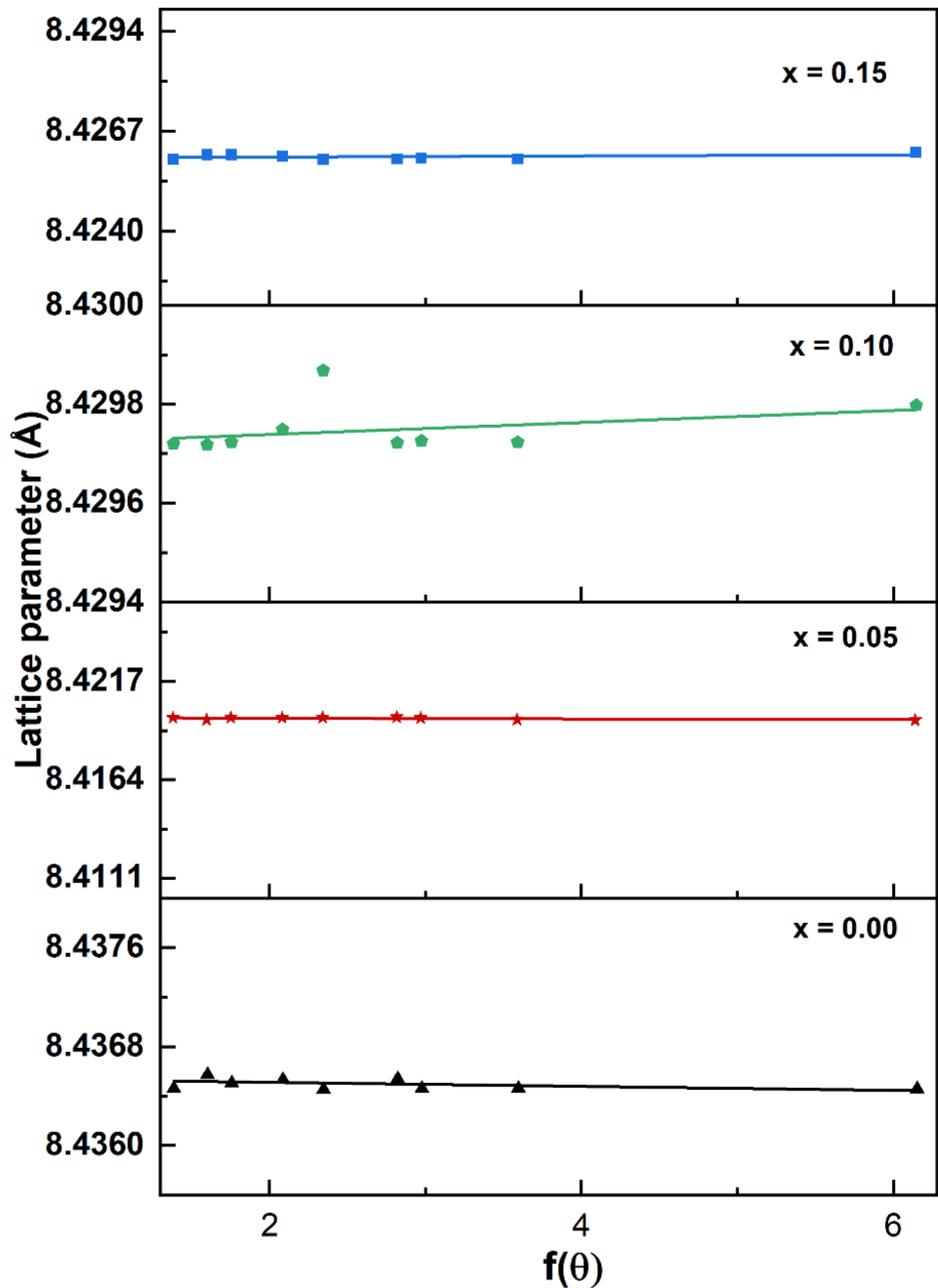

Fig. 1 X-ray intensity, peak shift

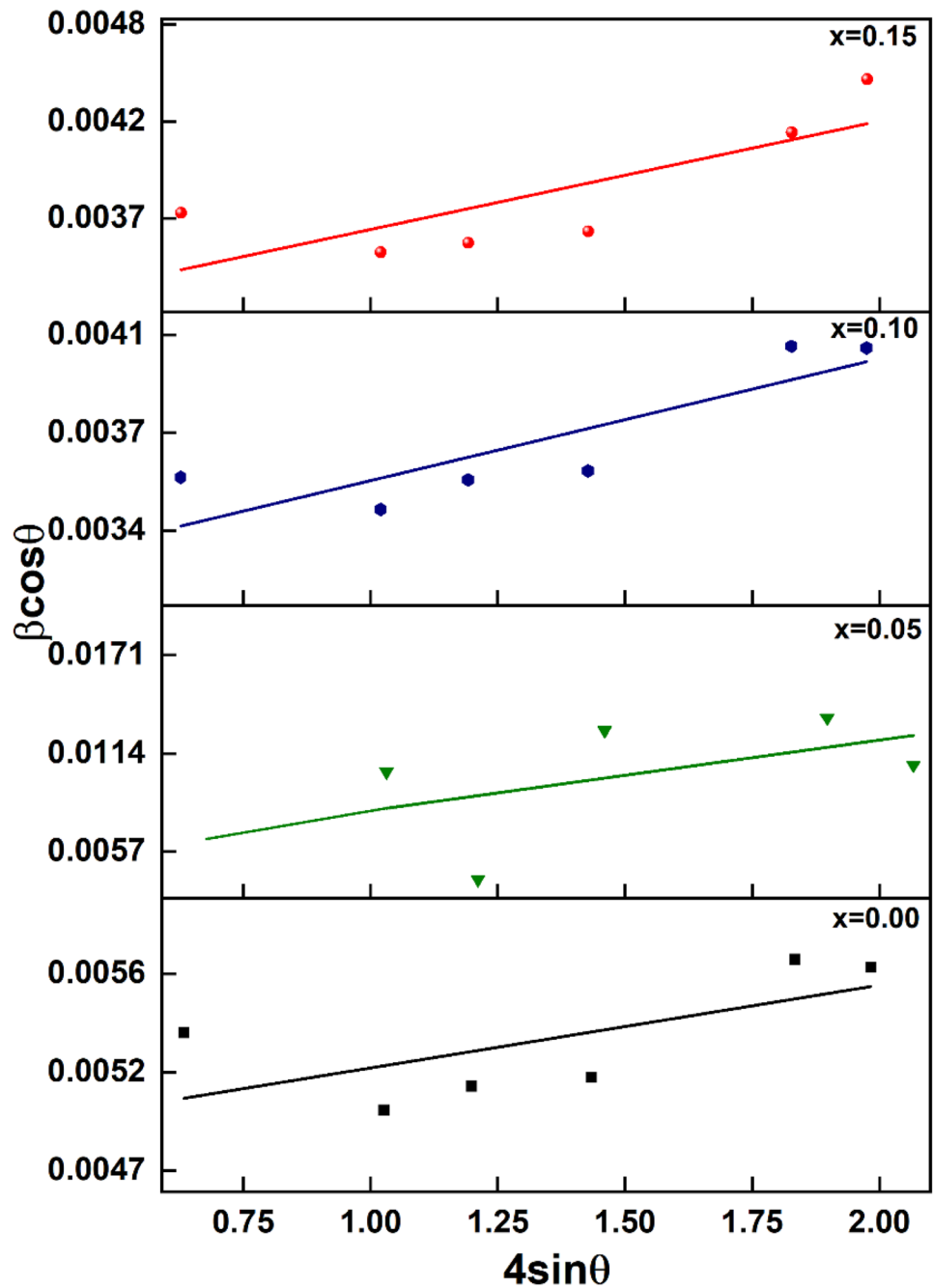**Fig. 2** Nelson–Riley plot, lattice parameter

The precise cell parameters of all the compositions of the samples were determined using Nelson–Riley plot (Fig. 2) which is a graph drawn between $f(\theta)$ and lattice parameter, where $f(\theta) = (\cos^2\theta/\sin\theta) + (\cos^2\theta/\theta)$ [35, 36]. Williamson–Hall plot was used for the crystallite size and lattice strain estimation. The crystallite size (D) and lattice strain (η) are estimated by the following formula [37]:

$$\beta cos\theta = 4\eta sin\theta + K\lambda/D \qquad (1)$$

Here, β represents the full width at half maximum (FWHM), θ the diffraction angle and λ the wavelength of X-ray. Figure 3 shows the plot of $4\sin\theta$ versus $\beta\cos\theta$, which is a straight-line giving slope η, lattice strain and intercept $K\lambda/D$ (D-crystallite size).

The calculated lattice parameter, estimated average crystallite size and lattice strain by various methods are reported in Table 1. The increasing trend of lattice parameters with Zn^{2+} doping is confirmed by unit cell refinement and the

Fig. 3 Williamson–Hall plot-crystallite size and lattice strain

Table 1 Average structural parameters refined from raw XRD data

$Zn_xCa_{1-x}Fe_2O_4$	Lattice parameter (Å)	Average crystallite size (nm)		Lattice strain (10^{-4})
	Nelson–Riley plot	Debye–Scherrer formula	Williamson–Hall plot	Williamson–Hall plot
$x=0.0$	8.4365	22	28	3.96
$x=0.05$	8.4197	24	34	4.08
$x=0.1$	8.4297	39	43	4.24
$x=0.15$	8.4259	31	44	5.91

Nelson–Riley method. The estimated average crystallite size varies from 22 to 44 nm by Debye and Williamson approaches. The micro lattice strain has minimum and maximum values of 3.96×10^{-4} and 5.91×10^{-4} for the composition $CaFe_2O_4$ and $Zn_{0.15}Ca_{0.85}Fe_2O_4$, respectively. It is found that the lattice strain increases with Zn^{2+} doping.

3.1.2 Cation Distribution Analysis

X-ray intensity analysis is one of the best methods to locate the distribution of cations in both tetrahedral A site and octahedral B site, with the assumption [38–40]

$$\left(Zn_a^{2+}Ca_\beta^{2+}Fe_{1-a\beta^{3+}}\right)^A \left[Zn_{x-a^{2+}}Ca_{1-x-\beta^{2+}}Fe_{1-a\beta^{3+}}\right]^B O_4^{2-} \quad (2)$$

where α and β are the distribution of Zn^{2+} and Ca^{2+} in A site, respectively. Comparing both observed and theoretical model-based intensities for various cation active lattice planes gives the cation distribution. The theoretical intensity in tetrahedral A and octahedral B sites was computed using the following equation [41]:

$$I_{hkl} = |F_{hkl}|^2 L_p \, P_{hkl} \quad (3)$$

with I_{hkl} is the calculated intensity of the lattice plane (hkl), F_{hkl} the structure factor, L_p the Lorentz polarisation factor and P_{hkl} the multiplicity factor. The ratios of the observed X-ray intensity and theoretical intensity I_{220}/I_{400}, I_{220}/I_{440}, I_{400}/I_{440} and I_{400}/I_{422} for the highly sensitive (hkl) planes (220), (440) and (400), (422) [41] were compared. The closely matched observed and calculated intensity ratios confirmed the occupation of tetrahedral A and octahedral B sites. Table 2 gives the cation distribution analysis based on the X-ray intensity data. It is found from Table 2 that Fe^{3+} and Ca^{2+} are partially distributed at both the tetrahedral A and octahedral B sites. As Zn^{2+} doping concentration is increased, there is a tendency of Zn^{2+} to move from tetrahedral A to octahedral B site. Complete inclusion of Zn^{2+} ions at octahedral B site is found for the composition $x = 0.15$. This result contradicts the earlier reports stating that Zn^{2+} always prefer to be in tetrahedral A site [42].

The refined structural parameters like distances between cations (Me-Me) and between cations and anions (Me-O) and interatomic angles based on cation distribution analysis of $Zn_xCa_{1-x}Fe_2O_4$ among the tetrahedral A and octahedral B sites are given in Table 3. The tetrahedral A site radius has the maximum value, 0.82655 nm, and octahedral B site radius has the minimum value, 0.6021 nm, for the composition, $x = 0.1$. The hopping length of the tetrahedral A site (L_A) and octahedral B site (L_B) has random variation with doping concentration. It is also found that L_A is greater than L_B, for all compositions as per the earlier reports [43]. All the above variations may be attributed to the random distribution of different ionic radii of dopant ion Zn^{2+} (0.74 Å) and host ion Ca^{2+} (0.99 Å) in tetrahedral A and octahedral B sites and the variation in occupational oxygen parameters.

3.1.3 Optical Bandgap Analysis

UV–Visible spectroscopy is the absorption of the ultraviolet and visible part of the electromagnetic radiation by the sample's ions or atoms or molecules due to the transition between two energy states. This absorption of UV and visible light analysis can help calculate the crystalline materials' optical bandgap. The deuterium lamp is a source of the ultraviolet light, and the tungsten lamp acts as a source of the visible light. The wavelength ranging from 2000 to 8000 Å with step size 2 Å was utilised for the analysis. Tauc plot method was used for the calculation of optical bandgap by plotting energy (eV) in the x-axis and $(\alpha h\nu)^2$ and (eV cm^{-1})^2 in the y-axis [44]. Figure 4 gives the graph for calculating the optical bandgap, and the inset presents the original absorption curve. The minimum and maximum observed bandgap energy is 2.8681 eV for the composition $x = 0.0$ and 2.9768 eV for the composition $x = 0.10$. The bandgap gradually increases as Zn^{2+} doping concentration is increased up to $x = 0.10$, reaches a maximum and then decreases beyond this ($x = 0.15$). The above trend may be due to the localised nature of the electron density distribution, which is also revealed by 3D and 2D MEM results.

Table 2 Estimated cation distribution among tetrahedral A and octahedral B site using X-ray intensity data

Sample name	Cation active intensity ratios						Tetrahedral A site occupancy	Octahedral B site occupancy
	I_{220}/I_{400}		I_{400}/I_{440}		I_{220}/I_{440}			
	Cal	Obs	Cal	Obs	Cal	Obs		
$CaFe_2O_4$	1.379	1.375	0.914	0.905	1.261	1.246	$(Ca_{0.59}Fe_{0.41})^A$	$(Ca_{0.41}Fe_{1.59})^B$
$Zn_{0.05}Ca_{0.95}Fe_2O_4$	1.716	1.774	0.804	1.041	1.379	1.847	$(Zn_{0.04}Ca_{0.285}Fe_{0.675})^A$	$(Zn_{0.01}Ca_{0.665}Fe_{1.325})^B$
$Zn_{0.10}Ca_{0.90}Fe_2O_4$	1.696	1.702	0.805	0.891	1.366	1.517	$(Zn_{0.01}Ca_{0.245}Fe_{0.745})^A$	$(Zn_{0.09}Ca_{0.655}Fe_{1.255})^B$
$Zn_{0.15}Ca_{0.85}Fe_2O_4$	1.741	1.536	0.795	0.875	1.385	1.344	$(Zn_{0.00}Ca_{0.165}Fe_{0.835})^A$	$(Zn_{0.15}Ca_{0.685}Fe_{1.165})^B$

Table 3 Interatomic distances between cations (Me-Me), between anions and cations (Me-O) and interatomic angles of $Zn_xCa_{1-x}Fe_2O_4$, $x = 0.0$, 0.05, 0.1, 0.15

Calculated parameters		$x = 0.00$	$x = 0.05$	$x = 0.10$	$x = 0.15$
Tetrahedral A site (Å)	Radii r_A	0.6527	0.5467	0.8265	0.6649
	Shared edge length d_{AE}	3.2215	3.0484	3.5052	3.2413
	Hopping length (Å)	3.6532	3.6460	3.6505	3.6487
Octahedral B site (Å)	Radii r_B	0.7048	0.7597	0.6021	0.6939
	Shared edge length d_{BE}	2.7442	2.9055	2.4560	2.7170
	Unshared edge length d_{BEU}	2.9876	2.9773	3.0036	2.9849
	Hopping length (Å)	2.9828	2.9769	2.9806	2.9791
Interatomic distances and angles					
M_e-M_e (Å)	b	2.9828	2.9769	2.9806	2.9791
	c	3.4977	3.4907	3.4951	3.4934
	d	3.6532	3.6460	3.6505	3.6487
	e	5.4799	5.4690	5.4758	5.4731
	f	5.1665	5.1562	5.1626	5.1601
M_e-O (Å)	p	2.0235	2.0796	1.9145	2.0123
	q	1.9750	1.8669	2.1596	1.9876
	r	3.7819	3.5749	4.1354	3.8061
	s	3.7025	3.6606	3.7620	3.7031
Angles (°)	θ_1	122°01'	124°17'	118°01'	121°41'
	θ_2	139°27'	149°26'	125°35'	138°11'
	θ_3	94°57'	91°24'	102°13'	95°30'
	θ_4	126°22'	125°35'	127°49'	126°29'
	θ_5	71°01'	77°08'	61°48'	70°12'

Fig. 4 UV–Visible spectrum, bandgap
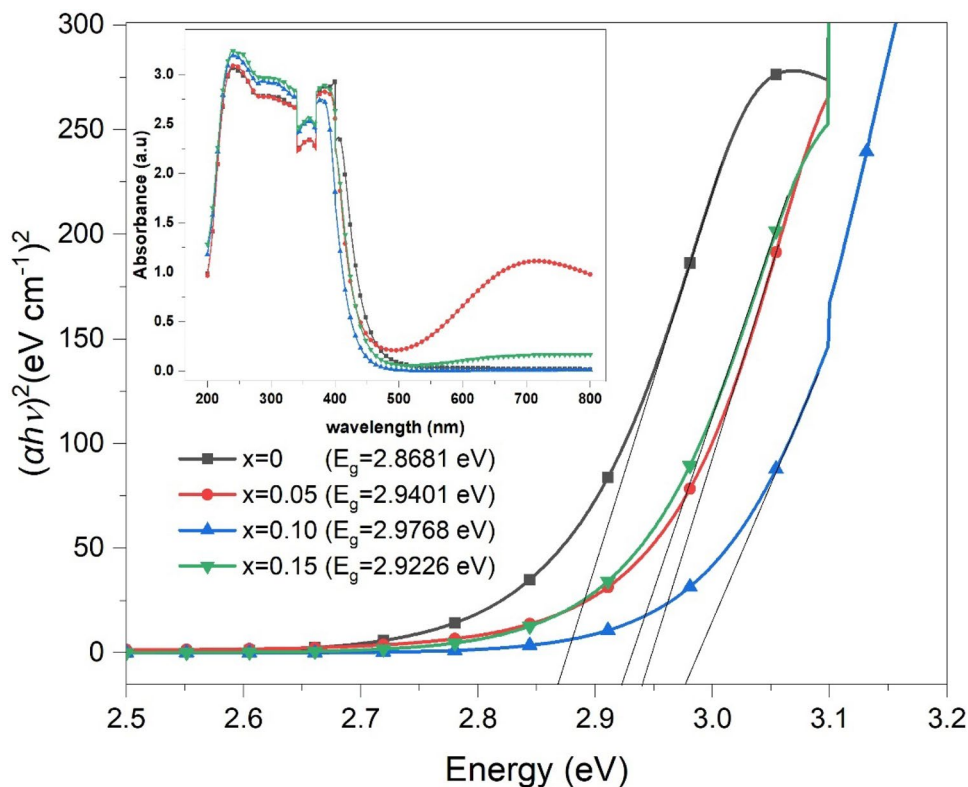
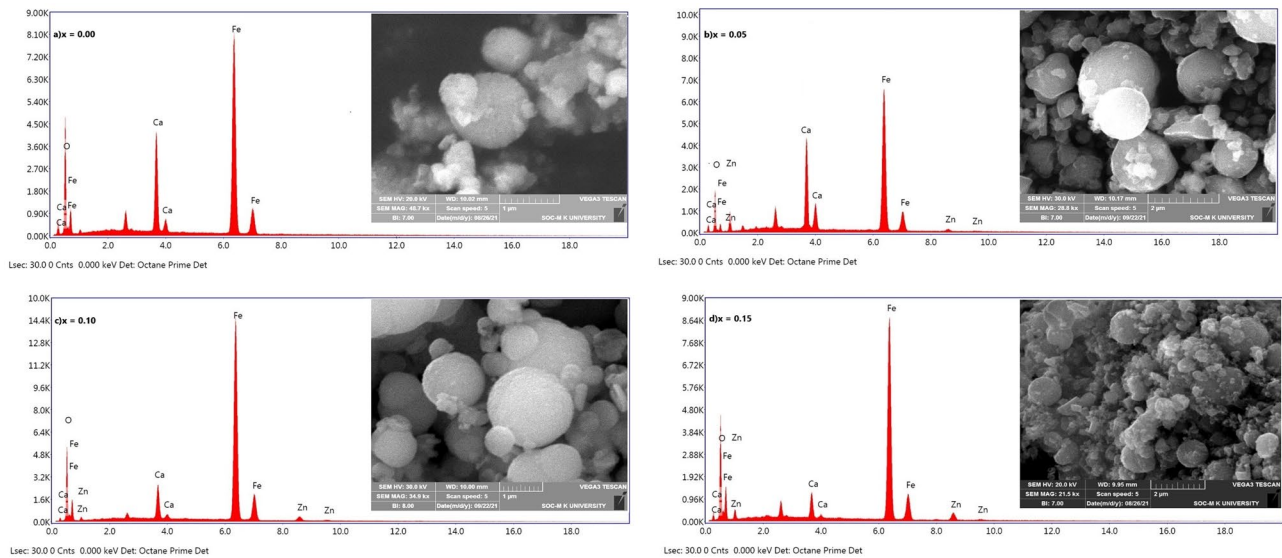**Fig. 5** EDX analysis of $Zn_xCa_{1-x}Fe_2O_4$ with inset in the SEM image for the composition (**a**) x = 0.00, (**b**) x = 0.05, (**c**) x = 0.10, and (**d**) x = 0.15

3.1.4 SEM/EDX Analysis

All the compositions of the prepared samples were analysed for surface morphology and elemental composition using scanning electron microscopy (SEM) and energy-dispersive X-ray (EDX) analysis. The maximum magnification of 70 kX with a potential of 30 kV was used for the SEM analysis. Figure 5a, b, c and d shows the EDX graph with an inset showing their corresponding SEM image. SEM image shows the spherical nature of the particles in all compositions of the samples, with the exception that the composition $x = 0.15$ has some agglomerate. The relative proportions of the elemental

Fig. 6 VSM graph of $Zn_xCa_{1-x}Fe_2O_4$ with the inset its enlarged version ($x = 0.0, 0.05, 0.10, 0.15$)
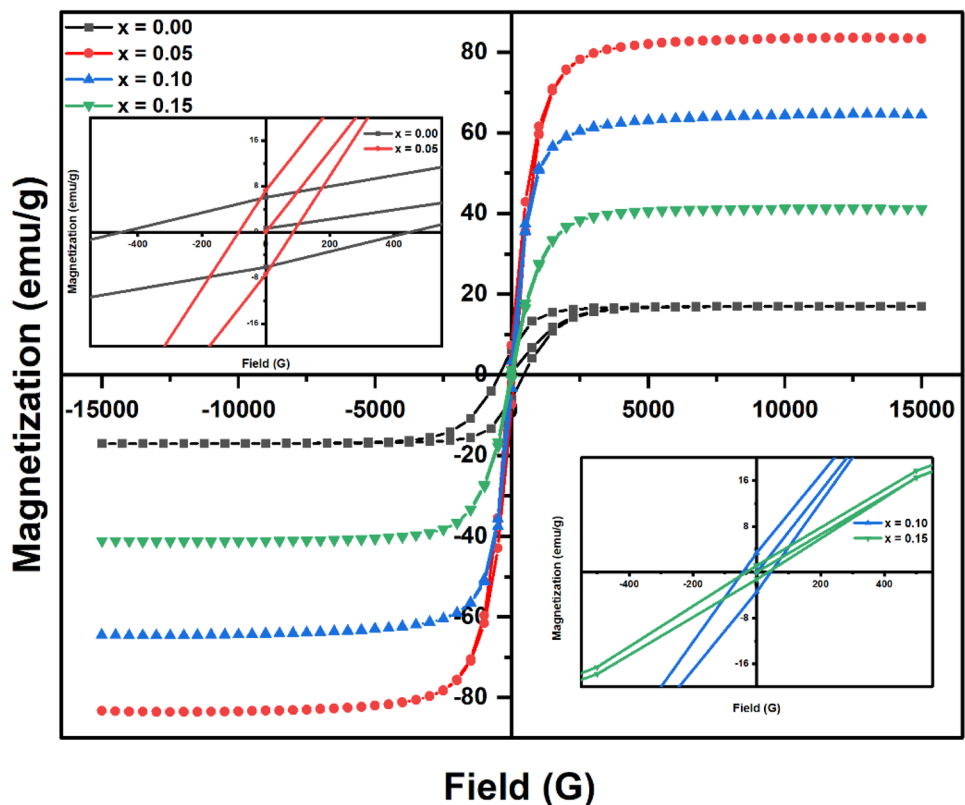
Table 4 Experimental magnetic parameters from VSM

Sample $Zn_xCa_{1-x}Fe_2O_4$	Magnetisation (M_s) (emu/g)	Coercivity (H_{ci}) (G)	Retentivity (M_r)(emu/g)	Squareness ratio (M_r/M_s)	μ_B^H	μ_B^N
$x=0.0$	16.99	450.54	6.0909	0.358	0.656	0.650
$x=0.05$	83.59	85.537	7.338	0.090	3.248	3.250
$x=0.10$	64.65	43.280	3.3757	0.052	2.527	2.550
$x=0.15$	41.27	33.127	1.1754	0.028	1.622	1.650

composition of Zn, Ca, Fe and O are seen in all the compositions ($Zn_xCa_{1-x}Fe_2O_4$, $x=0.0$, 0.05, 0.10, 0.15) of the prepared samples, along with an additional peak corresponding to chlorine atoms, which arises due to the addition of concentrated HCl acid at filtration process of sample preparation. EDX reveals the perfect doping of Zn^{2+} in the host Ca^{2+}.

3.1.5 Magnetic Hysteresis Analysis

Magnetic properties like saturation magnetic moment (M_s), remanent magnetic moment (M_r), coercivity (H_{ci}) and squareness ratio (M_r/M_s) of the prepared samples were analysed at room temperature using the hysteresis curve analysis by VSM. Figure 6 shows the hysteresis curve with the inset and its expanded view, and Table 4 gives the observed magnetic parameters for all compositions of $Zn_xCa_{1-x}Fe_2O_4$ ($x=0.0$, 0.05, 0.1, 0.15). It is found that the composition $x=0.0$ has minimum saturation magnetisation and maximum

coercivity. The *Ms* value increases with doping, reaches a maximum for the composition $x=0.05$ and decreases with further doping. All the compositions behave like soft ferrites with moderate saturation magnetisation and coercivity. The maximum squareness ratio is 35.8% for the composition $x=0.0$ [20]. It is also observed from the table (VSM) that there is a slow switching behaviour from soft ferromagnetism to super paramagnetism as the Zn^{2+} concentration increases. The above switching may be due to the shifting of magnetic Fe^{3+} ions from octahedral B site to tetrahedral A site and the distribution of nonmagnetic Zn^{2+} ions in the B site according to the table (cation). Experimental Bohr magnetron (μ_B^H) values based on VSM analysis were calculated using the following formula [45]:

$$\mu_B^H = \frac{Molecular\ Weight}{5585} \times M_s \tag{4}$$

Table 5 Various structural refinement parameters of $Zn_xCa_{1-x}Fe_2O_4$, $x=0.0$, 0.05, 0.1, 0.15

Parameters	Values	$x=0.00$	$x=0.05$	$x=0.10$	$x=0.15$
Refined structural parameters					
Lattice parameters (Å)	a	8.4369(2)	8.4201(4)	8.4306(2)	8.4264(5)
Volume of the unit cell (Å^3)	a^3	600.55	596.9	599.21	598.31
X-ray density (g/cm^3)	D_x	4.7726	4.8293	4.8394	4.8747
Oxygen positional parameter	$U^{\overline{4}3m}$	0.385(8)	0.378(7)	0.397(1)	0.386(3)
Rietveld reliability indices					
Reliability index	R_{obs} (%)	5.07	6.46	5.80	7.10
Weighted reliability index	wR_{obs} (%)	2.84	10.9	5.69	5.11
R_{all} (%)		6.59	8.64	11.8	8.14
wR_{all} (%)		2.98	10.9	6.18	5.21
Profile reliability index	R_p (%)	2.29	3.34	2.81	2.52
Weighted profile reliability index	wR_p (%)	2.92	4.49	3.76	3.26
Goodness of fit	GOF	1.02	1.08	1.08	1.02
No. of electrons/unit cell	F_{000}	832	836	840	844
MEM parameters and reliability indices					
No. of cycles		1677	2155	3334	1672
No. of pixels/unit cell		2097152	2097152	2097152	2097152
Prior density (e/Å^3)	F_{000}/a^3	1.3852	1.4003	1.4018	1.4106
Lagrange parameter	λ	0.0106	0.0177	0.0559	0.0106
Reliability index	R_{MEM}(%)	6.83	10.02	8.80	6.90
Weighted reliability index	wR_{MEM}(%)	3.07	4.00	2.99	3.32

The theoretical value of model-based Bohr magnetron was calculated from cation distribution analysis and Neel's two sublattices' model using the relation $\mu_B{}^N = M_B - M_A$, where M_B is the B site magnetisation and M_A is the A site magnetisation. Both experimental and theoretical Bohr magnetron values are well-matched, obeying Neel's two sublattices' collinear model.

3.2 Computational Analysis

3.2.1 Structural Analysis

All compositions of the prepared samples were analysed using the powder profile fitting method called Rietveld refinement technique using the JANA 2006 [25, 30]. The refined Rietveld parameters and reliability indices are shown in Table 5. The minimum reliability indices and goodness of fit show the perfectness of structural refinements and confirmation of the spinel ferrite structure. There is a random variation of both lattice parameter and volume of the unit cell by all methods of calculation. This may be because of the random distribution of lower ionic Zn^{2+} and higher ionic Ca^{2+} in tetrahedral A site and octahedral B site as reported in Table 2. Though there is a random variation in lattice parameter with doping concentration, the density linearly increases with doping. The occupational position of the oxygen ions also has the random variation and has the closest ideal value 0.378 for the composition $x = 0.1$. [32]. The number of charges inside a unit cell is given by F_{000}, which

has a linear increase from a minimum of 832 to a maximum of 844 with Zn^{2+} doping, which directly reveal the proper doping of high charge Zn atoms in low charge Ca atoms.

The weighted reliability indices are very small, and the goodness of fit (GOF) is nearly unity for all the compositions showing the perfectness of refinement. Figures 7, 8, 9 and 10 present the JANA2006 based Rietveld refinement profile fitting of observed (I_o) and calculated X-ray intensity (I_c), along with intensity difference ($I_o - I_c$) for all the compositions. The vertical lines coinciding the peaks represents the Bragg planes ($h\,k\,l$). The perfectness of refinement and validity of the proposed model (cubic spinel ferrite) are reflected in the profile diagrams. The expanded form of the profile fitting is given in the inset of each figure showing the significant peaks (113) and (222).

3.2.2 Electron Density Analysis

The experimental electron density distribution inside the unit cell is analysed using the mathematical tool, maximum entropy method. The XRD data based on structural parameters obtained from Rietveld refinements is utilised for the MEM electron density calculations using the software Dysnomia [46]. The resultant electron density on each pixel of the unit cell will be the outcome of the MEM calculations.

The obtained MEM parameters and reliability indices are given in Table 5. The 2D and 3D visual imaging of electron density was done using visualisation for electronic and structural analysis (VESTA) [33]. The 3D plot of charge density distribution with isosurfaces level $= 0.7$ e/Å^3, for the
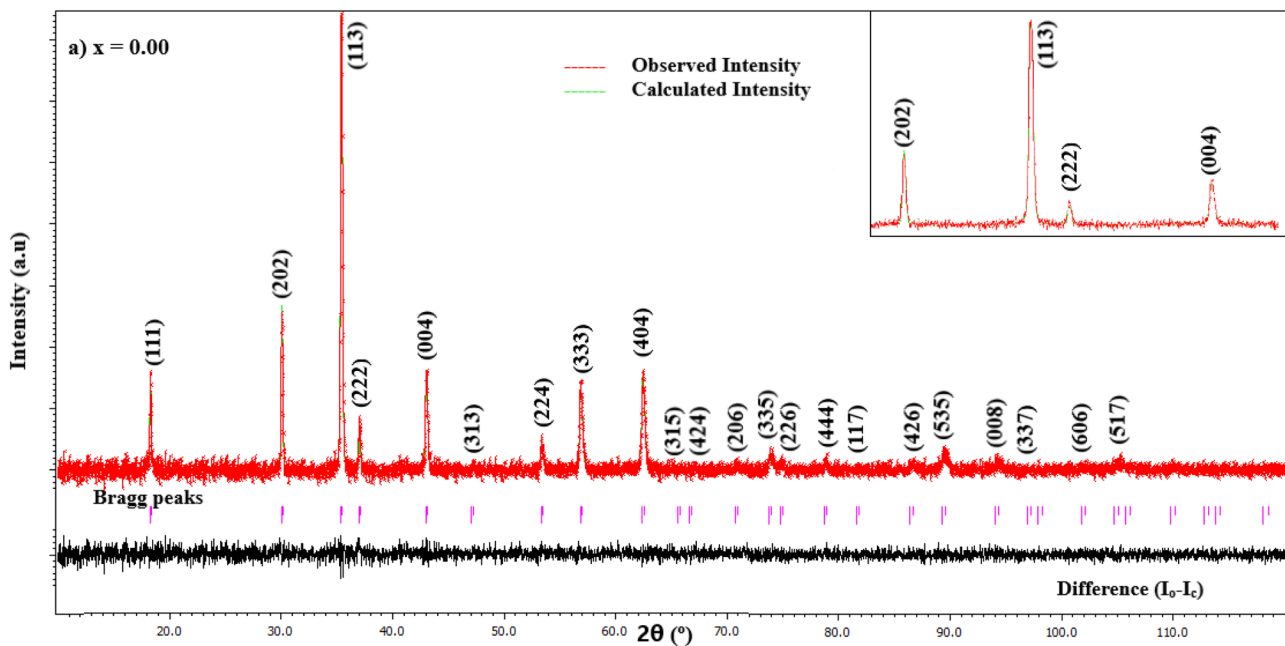

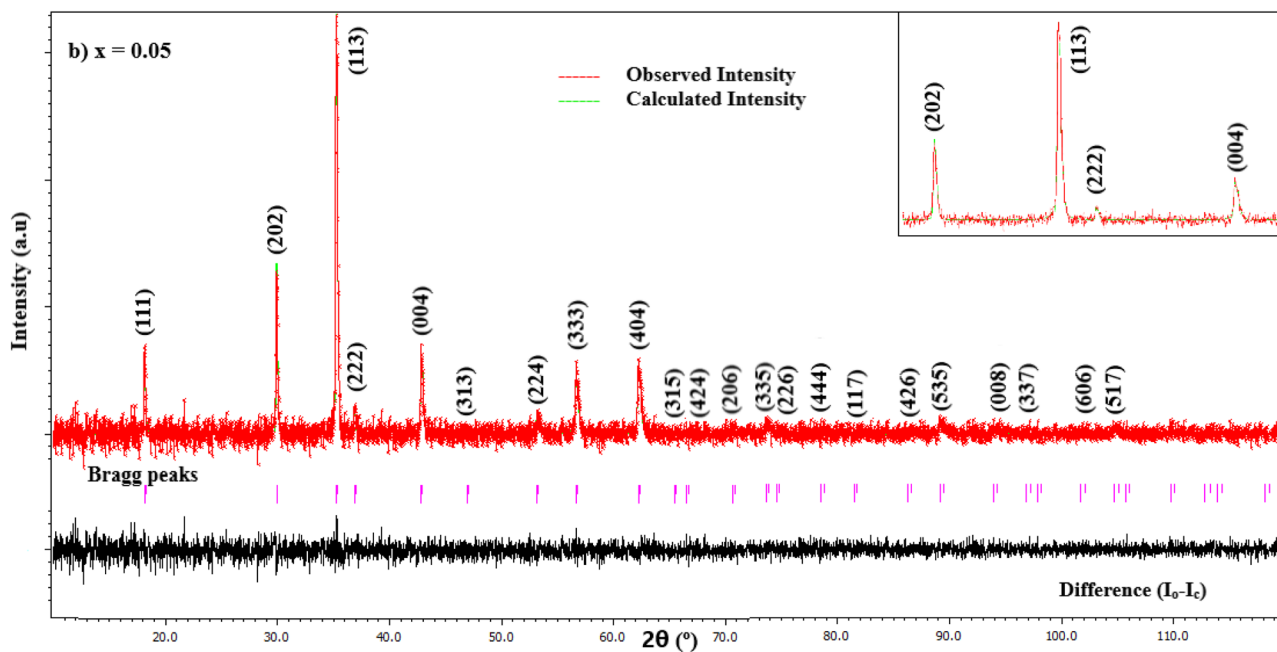**Fig. 7** JANA refined profile of $Zn_xCa_{1-x}Fe_2O_4$, $x = 0.0$, with inset its enlarged peaks

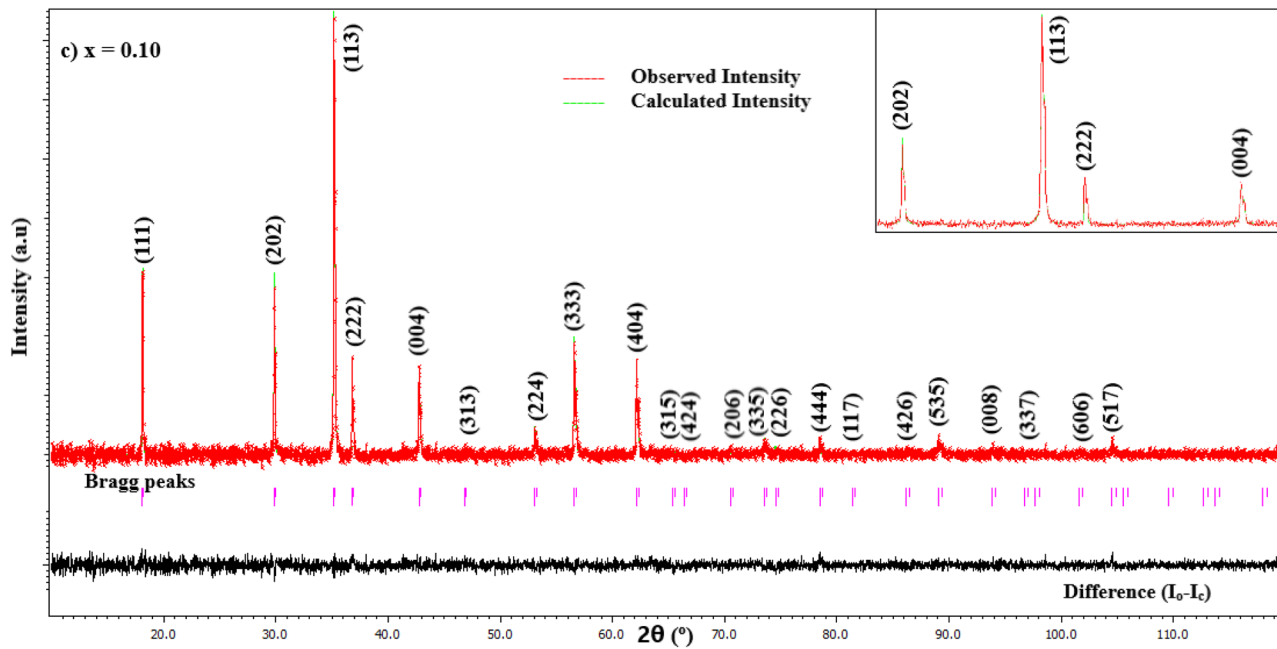**Fig. 8** JANA refined profile of $Zn_xCa_{1-x}Fe_2O_4$, $x = 0.05$, with inset its enlarged peaks

Fig. 9 JANA refined profile of $Zn_xCa_{1-x}Fe_2O_4$, $x = 0.10$, with inset its enlarged peaks

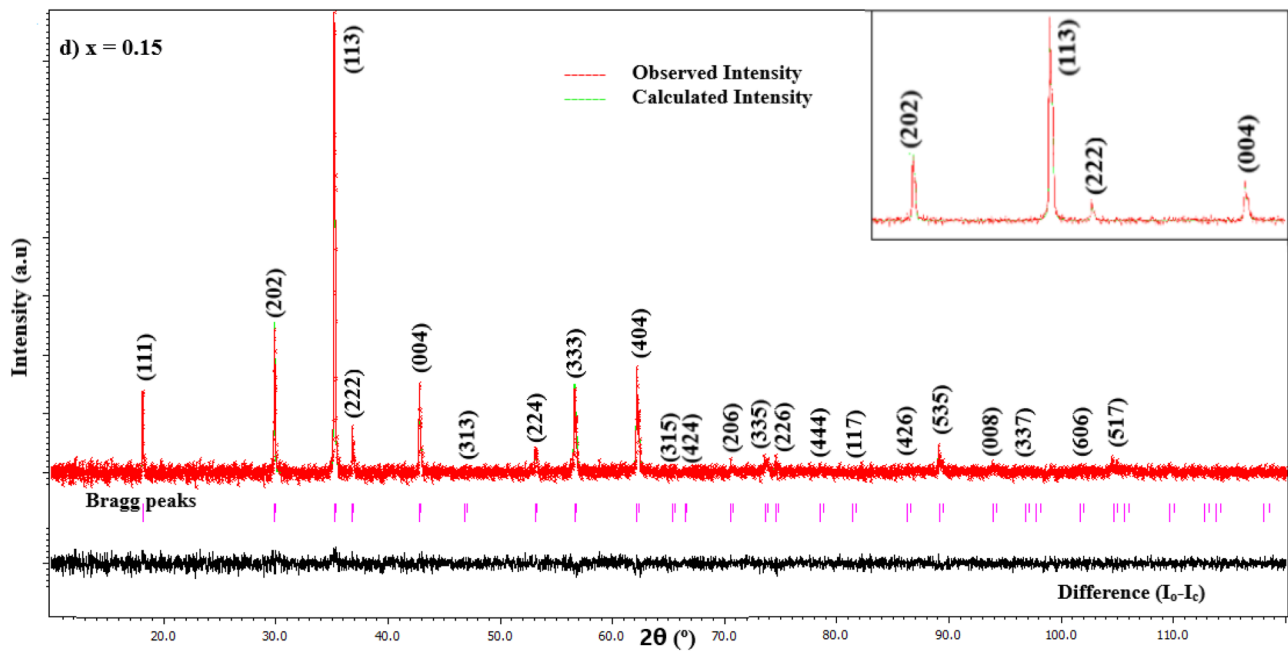**Fig. 10** JANA refined profile of $Zn_xCa_{1-x}Fe_2O_4$, $x=0.15$, with inset its enlarged peaks

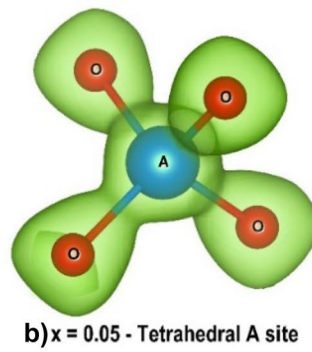**Fig. 11** 3D MEM electron density distribution of $Zn_xCa_{1-x}Fe_2O_4$, $x=0.05$ (isosurfaces level $0.7e/Å^3$)
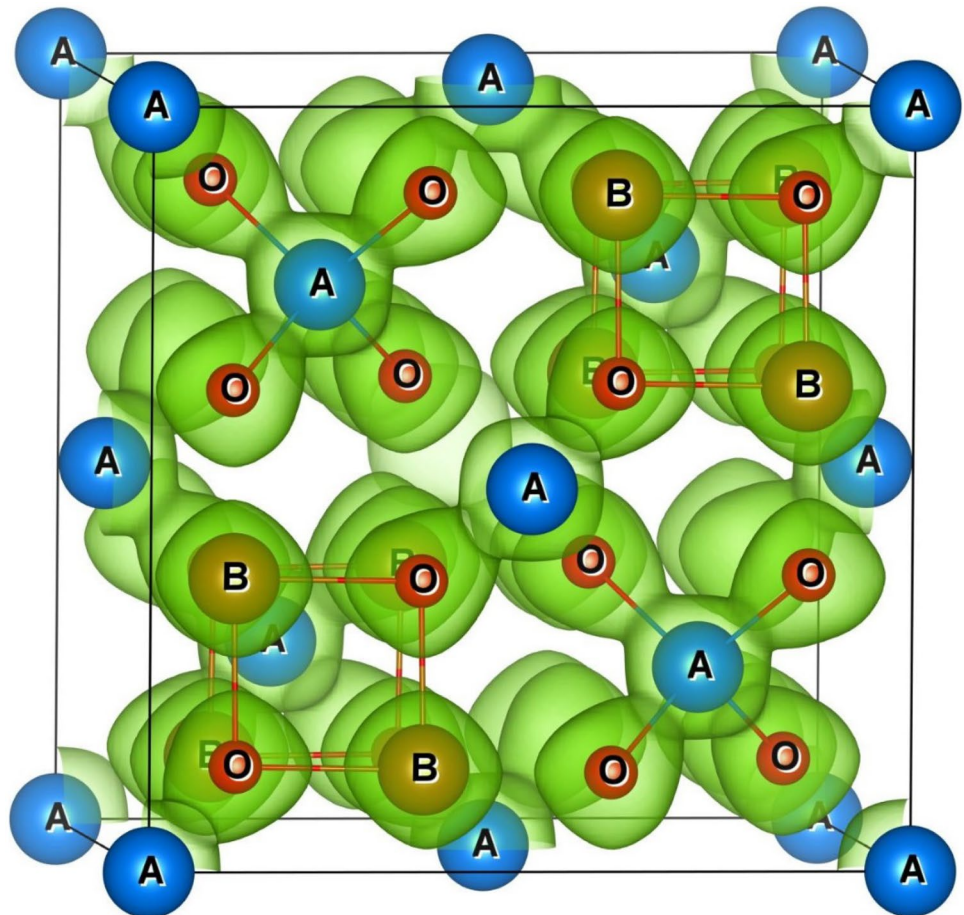
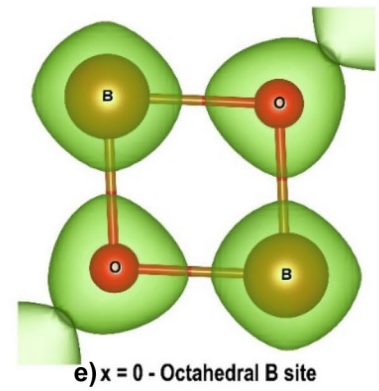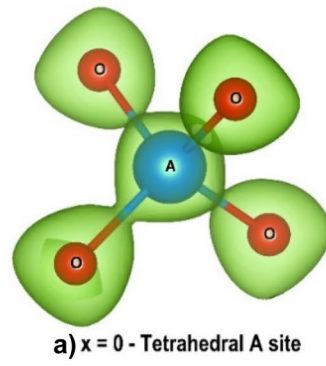**Fig. 12** 3D MEM electron density distribution of $Zn_xCa_{1-x}Fe_2O_4$ for the compositions $x = 0.0$, 0.05, 0.10, 0.15 showing, (**a-d**) tetrahedral A sites and (**e** - **h**) octahedral B sites (isosurface level 0.7 e/$\mathring{A}^3$)

a) x = 0 - Tetrahedral A site

e) x = 0 - Octahedral B site

b) x = 0.05 - Tetrahedral A site

f) x = 0.05 - Octahedral B site

c) x = 0.10 - Tetrahedral A site

g) x = 0.10 - Octahedral B site

d) x = 0.15 - Tetrahedral A site

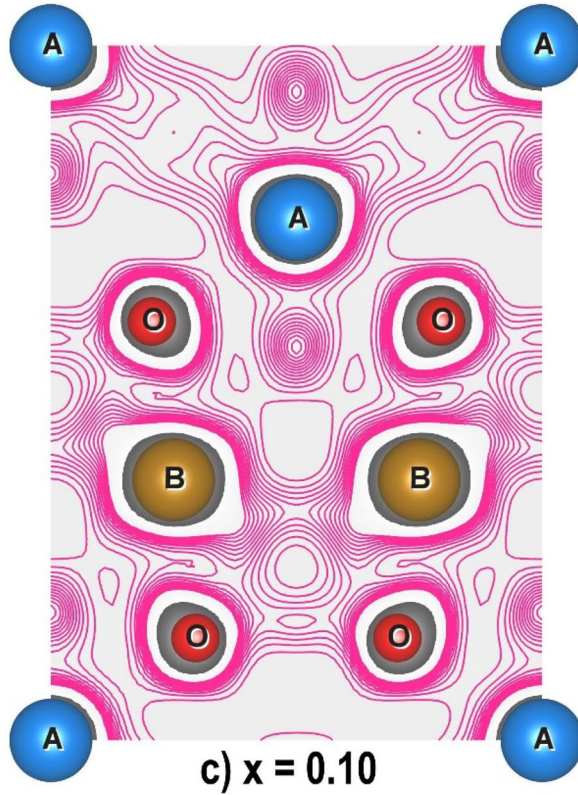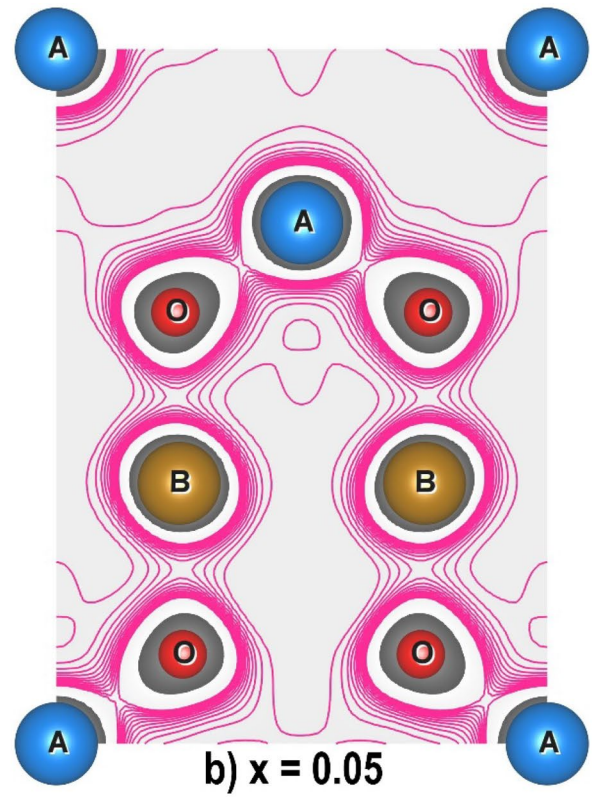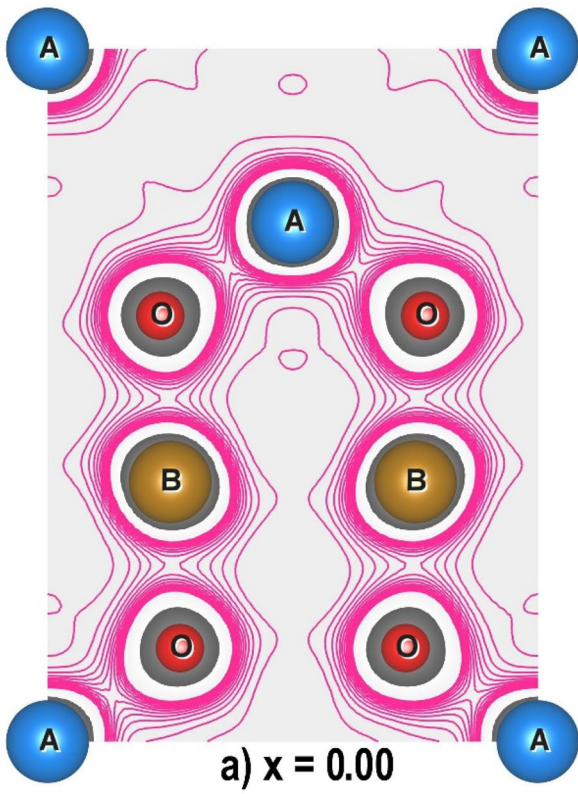h) x = 0.15 - Octahedral B site

a) x = 0.00
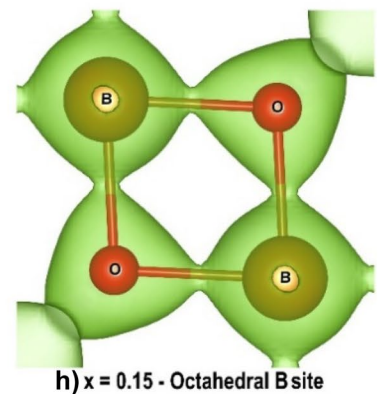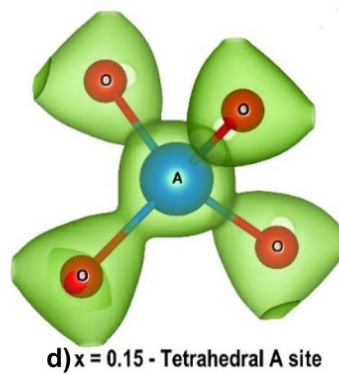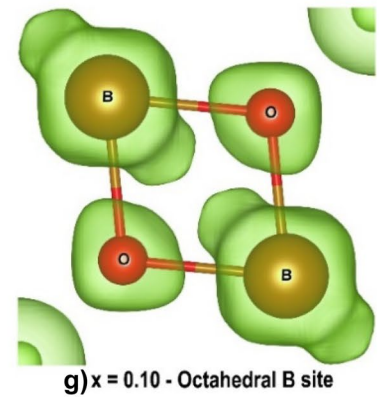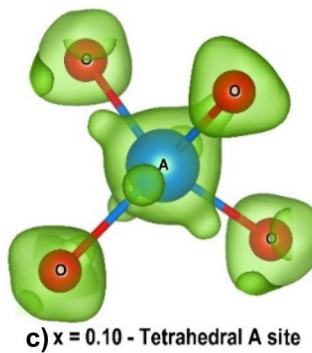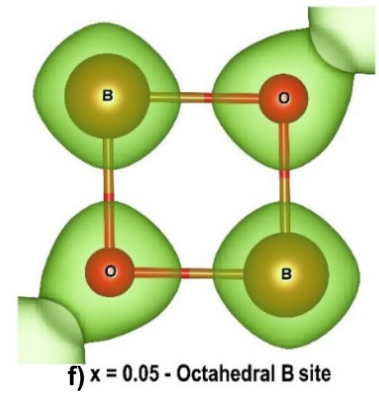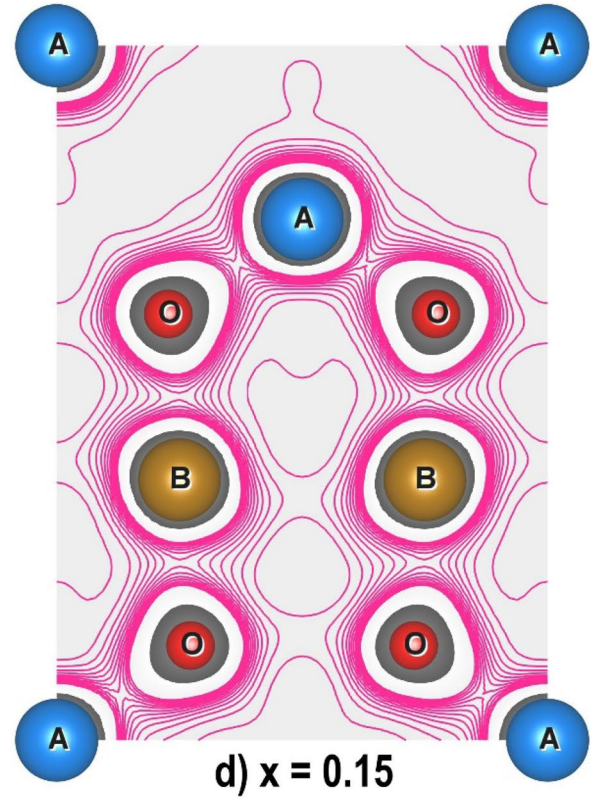
b) x = 0.05

c) x = 0.10

d) x = 0.15

◄**Fig. 13** 2D MEM electron density distribution of $Zn_xCa_{1-x}Fe_2O_4$ for the compositions, (**a**) $x=0.00$, (**b**) $x = 0.05$, (**c**) $x = 0.10$, (**d**) $x = 0.15$ along (110) plane with isosurface level 0.7 e/$\mathring{A}^3$, contour interval (0.17 to 1.49) e/$\mathring{A}^3$ and step size 0.1 e/$\mathring{A}^3$

composition $x=0.05$ is shown in Fig. 11 which shows the perfect spinel structure, with alternate tetrahedral A site and octahedral B site electron distribution.

Figure 12 shows the individual electron density distribution around the tetrahedral A and octahedral B sites and also the bonding between A–O and B–O for all the compositions of the sample, $Zn_xCa_{1-x}Fe_2O_4$ ($x=0.0, 0.05, 0.1, 0.15$). A comparative study of the tetrahedral interaction from Fig. 12a, b, c and d shows maximum bonding for the composition $x=0.05$, which is highly covalent in nature. There is highly localised electron density around A and O for the composition $x=0.1$ showing minimum A–O interaction, but there is a dominating A–A interaction. B–O interaction is the strongest for the composition $x=0.15$, which is visually seen from Fig. 12h. Maximum A–B and B–B interaction is seen from Fig. 12g for the composition $x=0.10$.

2D MEM electron density distribution of $Zn_xCa_{1-x}Fe_2O_4$ ($x=0.0, 0.05, 0.10, 0.15$), along (110) plane with isosurface level 0.7 e/$\mathring{A}^3$, contour interval (0.17 to 1.49) e/$\mathring{A}^3$ and step size 0.1 e/$\mathring{A}^3$ is shown in Fig. 13a, b, c and d. There is a bond stretching between A and O which is clearly seen through contour lines in Fig. 13b for the composition $x=0.05$. There is a favourable A–A and B–B interaction and very little A–O and B–O interaction also seen from Fig. 12c for the composition $x=0.10$.

The numerical 1D MEM electron density distribution and 1D MEM bonding profile between A–A, A–B, A–O, B–B, B–O and O–O are given in Table 6 and Fig. 14a, b, c, d, e and f, respectively. The numerical 1D results show that A–O interaction is covalent and most vital for $x=0.05$. No A–O bonding is seen in 2D, 3D and 1D for the composition $x=0.10$ (localised ionic bonding). B–O bonding has a covalent nature for $x=0.15$, and all others have ionic nature. The strongest A–A bonding and maximum A–O mid-bond length for the composition $x=0.10$ can be seen from 1D numerical and profile results.

Table 6 Numerical MEM 1D bond density of $Zn_xCa_{1-x}Fe_2O_4$, $x=0.0, 0.05, 0.10, 0.15$

| Sample name	$x=0.00$		$x=0.05$		$x=0.10$		$x=0.15$	
Parameters	Distance ($\mathring{A}$)	Mid-bond density (e/$\mathring{A}^3$)	Distance ($\mathring{A}$)	Mid-bond density (e/$\mathring{A}^3$)	Distance ($\mathring{A}$)	Mid-bond density (e/$\mathring{A}^3$)	Distance ($\mathring{A}$)	Mid-bond density (e/$\mathring{A}^3$)
A–A	1.82666	0.10894	1.53133	0.08791	1.8252	0.46867	1.82437	0.08472
A–B	2.18262	0.25772	2.24808	0.19287	1.80342	0.17391	1.97028	0.31258
A–O	0.97068	0.78832	0.90867	1.31453	1.14291	0.23985	0.94704	0.97648
B–B	1.49146	0.12659	1.48849	0.09321	1.49027	0.15653	1.48959	0.18003
B–O	0.98981	0.581	1.05365	0.50208	1.00054	0.46334	0.99174	0.74431
O–O	1.37202	0.1412	1.44407	0.09074	1.22643	0.40576	1.35469	0.20536
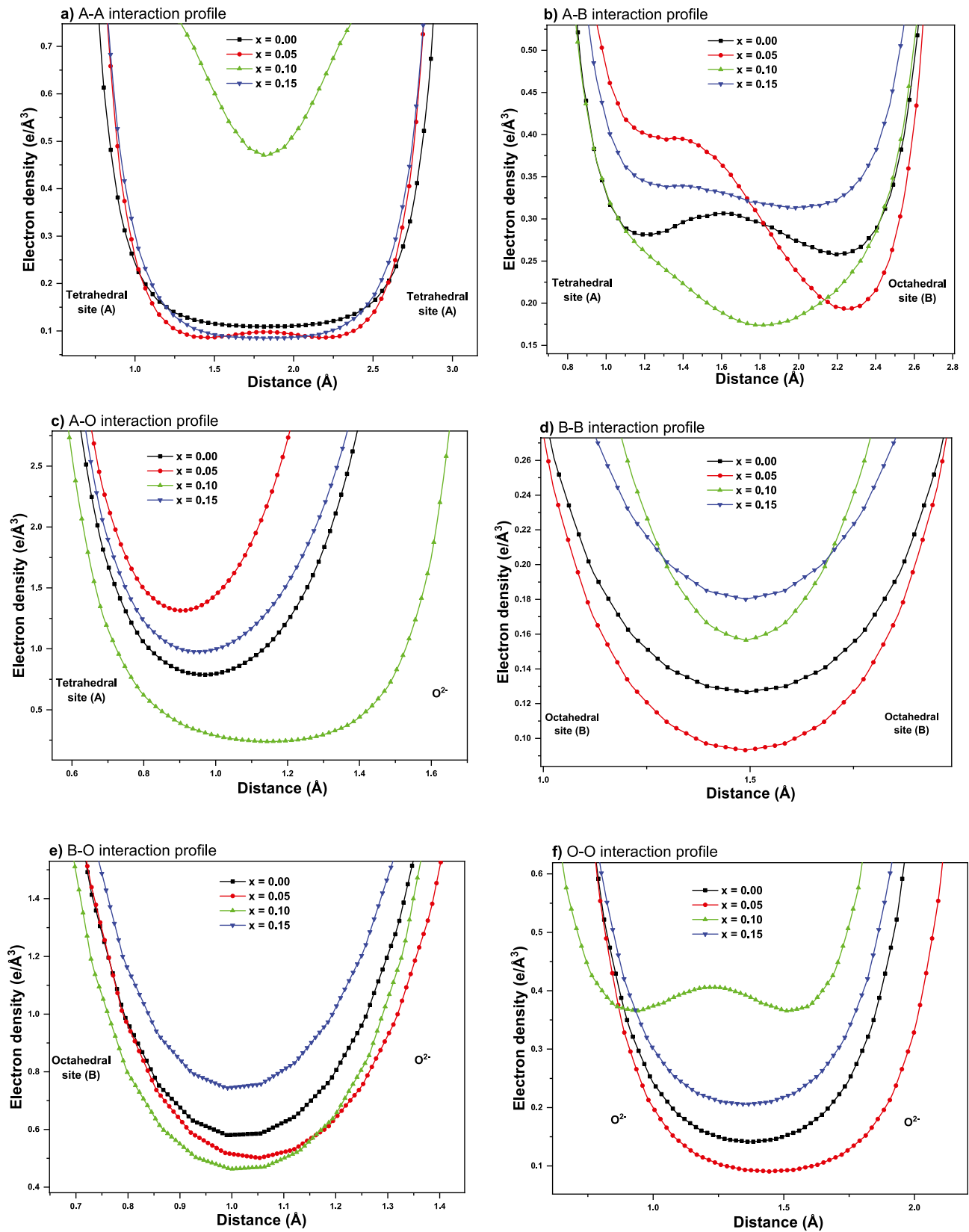
Fig. 14 1D MEM bond density distribution of $Zn_xCa_{1-x}Fe_2O_4$ for the compositions, $x = 0.00$, 0.05, 0.10, 0.15, showing (**a**) A–A, (**b**) A–B, (**c**) A–O, (**d**) B–B, (**e**) B–O and (**f**) O–O interaction profiles

4 Conclusion

Zn^{2+}-doped $CaFe_2O_4$ cubic spinel ferrites were prepared for the compositions $Zn_xCa_{1-x}Fe_2O_4$ ($x = 0.0, 0.05, 0.10, 0.15$) using low-temperature solvothermal method, and XRD peak analysis confirms the formation of single-phase spinel ferrite. Cation distribution analysis using both XRD methods and VSM (magnetic studies) shows mixed spinel formation with the occupation of host Ca^{2+} ions in the A and B site. The tendency of B site occupancy of all doped Zn^{2+} ions increases as the Zn^{2+} doping concentration increases. The optical bandgap varies in a random fashion with Zn^{2+} doping from 2.8681 to 2.9766 eV. The maximum coercivity and squareness ratio obtained for the composition $CaFe_2O_4$ is 405.54 G and 35.8%, respectively, which has the minimum average estimated crystallite size of 22 nm. The relation between maximum coercivity and minimum crystallite size may be due to the lowering of magnetic domains. The nonmagnetic Zn^{2+} doping decreases the overall magnetism. There is a slow switching behaviour from soft ferromagnetism to super paramagnetism observed as Zn^{2+} concentration increases, and the overall magnetism is well explained based on Neel's two sublattices' collinear model. The electron density distribution and bonding nature of the material are well established using MEM. The 3D, 2D and 1D MEM analysis reveals the weakest A–A bonding and also the alteration in A–B and B–B bond strength with doping. Moderate A–O and B–O covalent bonding favours maximum saturation magnetism of 83.59 emu/g for the composition $Zn_{0.05}Ca_{0.95}Fe_2O_4$.

Author Contribution M. Charles Robert, supervision, conceptualisation and methodology. M. Thavarani, investigation and writing original draft. N. Pavithra, executing graphical techniques and resources. S. Balaji Prasath, data curation, writing review and data analysis. R. Saravanan, formal analysis abd Software. Y. B. Kannan, electronic artwork and editing.

Data Availability The authors declare that all data supporting the findings of this study are available from the corresponding author with reasonable request.

Declarations

Conflict of Interest The authors declare no competing interests.

References

1. Candeia, R.A., Bernardi, M.I.B., Longo, E., Santos, I.M.G., Souza, A.G.: Synthesis and characterization of spinel pigment $CaFe_2O_4$ obtained by the polymeric precursor method. Mater. Lett. **58**, 569–572 (2004). https://doi.org/10.1016/S0167-577X(03)00563-9

2. Samariya, A., Dolia, S.N., Prasad, A.S., Sharma, P.K., Pareek, S.P., Dhawan, M.S., Kumar, S.: Size dependent structural and magnetic behaviour of $CaFe_2O_4$. Curr. Appl. Phys. **13**, 830–835 (2013). https://doi.org/10.1016/j.cap.2012.12.009

3. Tuna, Ö., Karadirek, Ş., Simsek, E.B.: Deposition of $CaFe_2O_4$ and $LaFeO_3$ perovskites on polyurethane filter: a new photocatalytic support for flowthrough degradation of tetracycline antibiotic. Environ. Res. **205**, (2022). https://doi.org/10.1016/J.ENVRES.2021.112389

4. Zhang, Z., Wang, W.: Solution combustion synthesis of $CaFe_2O_4$ nanocrystal as a magnetically separable photocatalyst. Mater. Lett. **133**, 212–215 (2014). https://doi.org/10.1016/j.matlet.2014.07.050

5. Knyazev, Y.V., Shishkina, N.N., Bayukov, O.A., Kirik, N.P., Solovyov, L.A., Zhizhaev, A.M., Rabchevsky, E.V., Anshits, A.G.: Cation distribution in the composite materials of the $CaFe_2O_4$-α-Fe_2O_3 series. J. Struct. Chem. **60**, 763–771 (2019). https://doi.org/10.1134/S0022476619050081

6. Kumar, D.S., Akhter, M., Ahmed, J., Amin, M.K., Kumar, D.P.: Synthesis and catalytic activity of spinel ferrites: a brief review. **12**, 4399–4416 (2022). https://doi.org/10.33263/BRIAC124.43994416

7. Borse, P.H., Kim, J.Y., Lee, J.S., Lim, K.T., Jeong, E.D., Bae, J.S., Yoon, J.H., Yu, S.M., Kim, H.G.: Ti-dopant-enhanced photocatalytic activity of a $CaFe_2O_4$/$MgFe_2O_4$ bulk heterojunction under visible-light irradiation. J. Korean Phys. Soc. **61**, 73–79 (2012). https://doi.org/10.3938/JKPS.61.73

8. Matsumoto, Y., Omae, M., Sugiyama, K., Sato, E.I.: New photocathode materials for hydrogen evolution: calcium iron oxide ($CaFe_2O_4$) and strontium iron oxide ($Sr_7Fe_{10}O_{22}$). J. Phys. Chem. **91**, 577–581 (2002). https://doi.org/10.1021/J100287A018

9. Lal, G., Punia, K., Dolia, S.N., Alvi, P.A., Dalela, S., Kumar, S.: Rietveld refinement, Raman, optical, dielectric, Mössbauer and magnetic characterization of superparamagnetic fcc-$CaFe_2O_4$ nanoparticles. Ceram. Int. **45**, 5837–5847 (2019). https://doi.org/10.1016/j.ceramint.2018.12.050

10. Kusaba, K., Yagi, T., Yamaura, J., Gotou, H., Kikegawa, T.: Under high pressure. J. Phys. Conf. Ser. **215**, 012001 (2010)

11. Debnath, A., Bera, A., Chattopadhyay, K.K., Saha, B.: Studies on magnetic properties of chemically synthesized crystalline calcium ferrite nanoparticles. AIP Conf. Proc. **1731**, 050103 (2016). https://doi.org/10.1063/1.4947757

12. da Silva, F.G., Depeyrot, J., Campos, A.F.C., Aquino, R., Fiorani, D., Peddis, D.: Structural and magnetic properties of spinel ferrite nanoparticles. J. Nanosci. Nanotechnol. **19**, 4888–4902 (2019). https://doi.org/10.1166/JNN.2019.16877

13. Jumril, Y., Noor Humam, S., Mariyam, J.G.: Synthesis of calcium ferrite nanoparticles ($CaFe_2O_4$-NPs) using auto-combustion method for targeted drug delivery. Key Eng. Mater. **775**, 115–119 (2018). https://doi.org/10.4028/WWW.SCIENTIFIC.NET/KEM.775.115

14. Khanna, L., Verma, N.K.: Size-dependent magnetic properties of calcium ferrite nanoparticles. J. Magn. Magn. Mater. **336**, 1–7 (2013). https://doi.org/10.1016/J.JMMM.2013.02.016

15. Jasso-Terán, R.A., Cortés-Hernández, D.A., Sánchez-Fuentes, H.J., Reyes-Rodríguez, P.Y., de-León-Prado, L.E., Escobedo-Bocardo, J.C., Almanza-Robles, J.M.: Synthesis, characterization and hemolysis studies of $Zn_{(1-x)}Ca_xFe_2O_4$ ferrites synthesized by sol-gel for hyperthermia treatment applications. J. Magn. Magn. Mater. **427**, 241–244 (2017). https://doi.org/10.1016/J.JMMM.2016.10.099

16. Goodarz Naseri, M., Saion, E.B., Kamali, A.: An overview on nanocrystalline $ZnFe_2O_4$, $MnFe_2O_4$, and $CoFe_2O_4$ synthesized by a thermal treatment method. ISRN Nanotechnol. **2012**, 1–11 (2012). https://doi.org/10.5402/2012/604241

17. Das, A.K., Govindaraj, R., Srinivasan, A.: Structural and magnetic properties of sol-gel derived CaFe$_2$O$_4$ nanoparticles. J. Magn. Magn. Mater. **451**, 526–531 (2018). https://doi.org/10.1016/J.JMMM.2017.11.102

18. Kheradmand, A., Vahidi, O., Masoudpanah, S.M.: Magnetic, hyperthermic and structural properties of zn substituted CaFe$_2$O$_4$ powders. Appl. Phys. A Mater. Sci. Process. **124**, (2018). https://doi.org/10.1007/S00339-018-1672-8

19. Ali, S.A., Matin, M.A., Hakim, M.A., Islam, M.F.: Effects of CoFe$_2$O$_4$ substitution on magnetic properties of NiFe2O4 spinel ferrite. IOP Conf. Ser. Mater. Sci. Eng. **438**, (2018). https://doi.org/10.1088/1757-899X/438/1/012017

20. Coey, J.M.D.: Noncollinear spin arrangement in ultrafine ferrimagnetic crystallites. Phys. Rev. Lett. **27**, 1140–1142 (1971). https://doi.org/10.1103/PhysRevLett.27.1140

21. Gowri, G., Saravanan, R., Srinivasan, N., Saravanan, O.V., Sonai, S.: Investigation on interatomic chemical bonding and charge-related optical, multiferroic properties of La1−xZnxFeO3 bulk ceramics. Mater. Chem. Phys. **267**, 124652 (2021). https://doi.org/10.1016/J.MATCHEMPHYS.2021.124652

22. Meenakshi, S.V., Saravanan, R., Srinivasan, N., Saravanan, O.V., Dhayanithi, D., Giridharan, N.V.: Charge density analysis, structural, electrical and magnetic studies of (1−x) BaTiO$_{3+x}$ NiFe$_2$O$_4$ ceramic composite. J. Electron. Mater. **49**, 7349–7362 (2020). https://doi.org/10.1007/S11664-020-08481-4

23. Kannan, Y.B., Saravanan, R., Srinivasan, N., Praveena, K., Sadhana, K.: Synthesis and characterization of some ferrite nanoparticles prepared by co-precipitation method. J. Mater. Sci. Mater. Electron. **27**, 12000–12008 (2016). https://doi.org/10.1007/s10854-016-5347-y

24. Saravanakumar, S., Sivaganesh, D., Ali, K.S.S., Robert, M.C., Rani, M.P., Chokkalingam, R., Saravanan, R.: Analysis of structural, optical and charge density distribution studies on Zn$_{1-x}$Mn$_x$S nanostructures. Phys. B Condens. Matter. **545**, 134–140 (2018). https://doi.org/10.1016/J.PHYSB.2018.05.037

25. Rietveld, H.M.: A profile refinement method for nuclear and magnetic structures. J. Appl. Crystallogr. **2**, 65–71 (1969). https://doi.org/10.1107/s0021889869006558

26. Gull, S.F., Daniell, G.J.: Nat. 1978 2725655 **272**, 686–690 (1978). https://doi.org/10.1038/272686a0

27. Kheradmand, A., Vahidi, O., Masoudpanah, S.M.: Magnetic, hyperthermic and structural properties of zn substituted CaFe$_2$O$_4$ powders. Appl. Phys. A. **124**, 1–7 (2018). https://doi.org/10.1007/S00339-018-1672-8

28. Blanco-Gutiérrez, V., Torralvo-Fernández, M.J., Sáez-Puche, R.: Magnetic behavior of ZnFe$_2$O$_4$ nanoparticles: effects of a solid matrix and the particle size. J. Phys. Chem. C. **114**, 1789–1795 (2010). https://doi.org/10.1021/JP908395V/SUPPL_FILE/JP908395V_SI_001.PDF

29. Zou, G., Li, H., Zhang, Y., Xiong, K., Qian, Y.: Solvothermal/hydrothermal route to semiconductor nanowires. Nanotechnology **17**, S313 (2006). https://doi.org/10.1088/0957-4484/17/11/S14

30. Petrícek, V., Dušek, M., Palatinus, L.: Crystallographic computing system JANA2006: General features. Zeitschrift fur Krist. **229**, 345–352 (2014). https://doi.org/10.1515/zkri-2014-1737

31. Lakhani, V.K., Pathak, T.K., Vasoya, N.H., Modi, K.B.: Structural parameters and X-ray Debye temperature determination study on copper-ferrite-aluminates. Solid State Sci. **13**, 539–547 (2011). https://doi.org/10.1016/J.SOLIDSTATESCIENCES.2010.12.023

32. Sickafus, K.E., Wills, J.M., Grimes, N.W.: Structure of spinel. J. Am. Ceram. Soc. **82**, 3279–3292 (1999). https://doi.org/10.1111/J.1151-2916.1999.TB02241.X

33. Momma, K., Izumi, F.: VESTA: A three-dimensional visualization system for electronic and structural analysis. J. Appl. Crystallogr. **41**, 653–658 (2008). https://doi.org/10.1107/S0021889808012016

34. Mangaiyarkkarasi, J., Saravanan, R., Ismail, M.M.: Chemical bonding and charge density distribution analysis of undoped and lanthanum doped barium titanate ceramics. J. Chem. Sci. **128**, 1913–1921 (2016). https://doi.org/10.1007/S12039-016-1190-1

35. Taylor, A., Sinclair, H.: On the determination of lattice parameters by the Debye-Scherrer method. Proc. Phys. Soc. **57**, 126–135 (1945). https://doi.org/10.1088/0959-5309/57/2/306

36. Nelson, J.B., Riley, D.P.: An experimental investigation of extrapolation methods in the derivation of accurate unit-cell dimensions of crystals. Proc. Phys. Soc. **57**, 160 (1945). https://doi.org/10.1088/0959-5309/57/3/302

37. Williamson, G.K., Hall, W.H.: X-ray line broadening from filed aluminium and wolfram. Acta Metall. **1**, 22–31 (1953). https://doi.org/10.1016/0001-6160(53)90006-6

38. Hua, J., Cheng, Z., Chen, Z., Dong, H., Li, P., Wang, J.: Tuning the microstructural and magnetic properties of CoFe$_2$O$_4$/SiO$_2$ nanocomposites by Cu2+doping. RSC Adv. **11**, 26336–26343 (2021). https://doi.org/10.1039/d1ra04763a

39. Waseda, Y., Shinoda, K., Sugiyama, K.: Cation distribution of ZnFe$_2$O$_4$ and CoFe$_2$O$_4$ spinels from anomalous X-ray scattering. Zeitschrift fur Naturforsch. - Sect. A J. Phys. Sci. **50**, 1199–1204 (1995). https://doi.org/10.1515/ZNA-1995-1226/MACHINEREADABLECITATION/RIS

40. Fritsch, D., Ederer, C.: Effect of epitaxial strain on the cation distribution in spinel ferrites CoFe$_2$O$_4$ and NiFe$_2$O$_4$: a density functional theory study. Appl. Phys. Lett. **99**, 1–9 (2011). https://doi.org/10.1063/1.3631676

41. Patange, S.M., Shirsath, S.E., Jadhav, S.S., Jadhav, K.M.: Cation distribution study of nanocrystalline NiFe$_{2-x}$Cr$_x$O$_4$ ferrite by XRD, magnetization and Mössbauer spectroscopy. Phys. Status Solidi Appl. Mater. Sci. **209**, 347–352 (2012). https://doi.org/10.1002/pssa.201127232

42. Akhtar, M.N., Yahya, N., Hussain, P.B.: Structural and magnetic characterizations of nano structured Ni$_{0.8}$Zn$_{0.2}$Fe$_2$O$_4$ prepared by self combustion method. Int. J. Basic Appl. Sci. **09**, 37–40 (2009)

43. Andhare, D.D., Jadhav, S.A., Khedkar, M.V., Somvanshi, S.B., More, S.D., Jadhav, K.M.: Structural and chemical properties of ZnFe$_2$O$_4$ nanoparticles synthesised by chemical co-precipitation technique. J. Phys. Conf. Ser. **1644**, (2020). https://doi.org/10.1088/1742-6596/1644/1/012014

44. Tong, S.K., Chi, P.W., Kung, S.H., Wei, D.H.: Tuning bandgap and surface wettability of NiFe$_2$O$_4$ driven by phase transition. Sci. Rep. **8**, 1–11 (2018). https://doi.org/10.1038/s41598-018-19319-9

45. Choodamani, C., Nagabhushana, G.P., Ashoka, S., Daruka Prasad, B., Rudraswamy, B., Chandrappa, G.T.: Structural and magnetic studies of Mg$_{(1-x)}$Zn$_x$Fe$_2$O$_4$ nanoparticles prepared by a solution combustion method. J. Alloys Compd. **578**, 103–109 (2013). https://doi.org/10.1016/J.JALLCOM.2013.04.152

46. Momma, K., Ikeda, T., Belik, A.A., Izumi, F.: Dysnomia, a computer program for maximum-entropy method (MEM) analysis and its performance in the MEM-based pattern fitting. Powder Diffr. **28**, 184–193 (2013). https://doi.org/10.1017/S088571561300002X